

Time domain simulations of piston-like resonant flow in the gap of an oscillating twin-hull using inviscid and viscous flow solvers

Patrick Marleaux*, Hendrik Simonis and Moustafa Abdel-Maksoud

Institute for Fluid Dynamics and Ship Theory, Hamburg University of Technology, Am Schwarzenberg-Campus 4, 21073 Hamburg, Germany

ARTICLE INFO

Keywords:

Nonlinear wave radiation
Multi-hull hydrodynamics
Helmholtz resonance
Wall effect
Mixed Eulerian Lagrangian
Volume of fluid

ABSTRACT

A numerical study of a semi-circular twin-hull section under heave oscillation is presented. Two different time domain simulation methods were used: Firstly, a boundary element method based on potential theory which incorporates fully nonlinear free surface boundary conditions by using a mixed Eulerian Lagrangian scheme. Secondly, a finite volume method in combination with a volume of fluid scheme for capturing the free surface. In order to evaluate the effects of viscosity, simulations with the finite volume method were carried out using inviscid as well as viscous flow assumptions. Hydrodynamic mass and damping coefficients were derived from first order Fourier coefficients and validated against results from linear theory and experiments. A detailed comparison of nonlinear results from both simulation methods was carried out in vicinity of the piston-mode resonance frequency and a very good agreement was found. The phase angles corresponding to the Fourier coefficients varied strongly with frequency, which went along with a phase shift of the fluid motion in the gap. Influence of viscosity on the flow was found to be present but had relatively low impact on the hydrodynamic forces.


1. Introduction

Many applications in the field of naval and ocean engineering are arranged in such a way, that vertical gaps occur within a floating structure or between adjacent structures. Examples for such arrangements are multi-hull ships, moonpools, side-by-side arrangement of vessels, multi-body offshore structures or ships in a terminal. Violent resonant fluid motion can occur within the gap of such an arrangement leading to heavy loads and potentially harming the safety of the operation. Different modes of resonance are possible depending on exciting frequency and gap size. In particular for narrow gap sizes the so-called piston-mode resonance, also known as Helmholtz or pumping mode resonance, has an pronounced effect on the hydrodynamic forces.

One of the earliest studies on that phenomena was conducted by Ohkusu (1969), who considered a pair of circular cylinders that were forced to heave harmonically on the free surface. Experimental results for the radiated wave height at a certain distance to the cylinders were compared with results from linearised potential theory using an extension of the solution procedure by Ursell (1949). A similar theoretical approach was used by Wang and Wahab (1971) who also carried out force measurements in a set of experiments using pairs of semi-circular cylinders. Hydrodynamic mass and damping coefficients were found to vary strongly close to resonance frequency with negative values for the added mass and damping coefficients close to zero.

Most of past investigations utilised frequency domain methods based on potential theory with linearised free surface boundary conditions to analyse the flow phenomena in gaps. A series of publications was devoted to the occurrence of so-called trapped wave modes (e.g. McIver (1996) and McIver et al. (2003)). For certain multi hull shapes no waves are radiated to infinity, which affects existence and uniqueness of solutions to the linear frequency-domain radiation problem. Molin (2001) developed a simplified formula for the piston-mode frequency of rectangular cylinders by treating the fluid in the gap like a rigid body. Also, for rectangular cylinders Yeung and Seah (2007) analysed free surface shapes and force coefficients at different resonant modes using a semi-analytical approach. A study by Faltinsen et al. (2007) showed that the free-surface elevation from linear theory inside a 2D moonpool at piston-mode resonance deviates significantly from experimental measurements. The authors suspected that free-surface nonlinearities were the main reason for these deviations. Porter and Evans (2011) as well as McIver and Porter (2016) established a wide-spacing approximation to derive hydrodynamic coefficients of an arbitrary shaped cylinder next to a wall in terms of

*Corresponding author

 patrick.marleaux@tuhh.de (P. Marleaux)
ORCID(s): 0000-0003-3830-6171 (P. Marleaux)

similar quantities for a single cylinder without a wall. A mathematical analysis regarding the sign of the added mass coefficients of two dimensional floating bodies, including twin-hulls, was conducted by McIver and McIver (2016).

As indicated by Faltinsen et al. (2007) nonlinear free surface effects may have an important effect on the hydrodynamic characteristics of a twin-hull. A possible way to account for these effects in the scope of potential flow is to utilize a boundary element method (BEM) with fully nonlinear free-surface boundary conditions and track the free surface in time domain using a mixed Eulerian Lagrangian (MEL) scheme. This method was applied to the radiation problem of twin-cylinders with rectangular and triangular cross sections by Maiti and Sen (2001). Significant influence of higher order force components were found especially for small water depth. However, the piston-mode phenomenon was not explicitly examined. Kristiansen and Faltinsen (2010) used a BEM/MEL approach to examine the motion of a rectangular ship section in a terminal when excited by an incoming wave. They implemented a vortex sheet tracking method to account for flow separation at the sharp edges of the body and found a significantly better agreement with experimental measurements compared to results without this technique. Li and Zhang (2016) proposed an alternative way to determine the resonance frequency of a twin-hull with a BEM/MEL technique. They simulated the gravity driven flow after an initial disturbance and evaluated dominant frequencies in the free surface elevation by means of a Fourier transformation.

While potential flow based methods usually offer relatively low computational costs, their main deficiency is that they rely on inviscid flow assumptions. Field based methods like the finite volume method (FVM) are able to solve the Navier-Stokes equations in a given fluid domain and thus include effects of viscosity in the simulation. In the context of piston mode resonance the most prominent effect of viscosity, which has been identified by past researches, is flow separation at the bilge keels. For instance, the work by Kristiansen and Faltinsen (2012) indicates that for the heave radiation problem of a box-shaped twin-hull even linearised free surface conditions may be sufficiently accurate as long as it is accounted for the vortex shedding at the bodies' edges. Based on a finite volume method (FVM) they propose a domain decomposition into a viscous regime around the edges and a potential flow domain everywhere else, including the free surface in the gap. Another example is Ananthakrishnan (2015) who simulated heave oscillations of a rectangular twin-hull with a finite difference method (FDM) incorporating viscous as well as inviscid flow assumptions. Pronounced differences between the respective results were evident in case of piston-mode resonance. The influence of viscosity motivated researchers to introduce empirical damping terms in the free surface boundary conditions of potential flow methods to increase their applicability for 3D side-by-side offloading scenarios (Zhao et al., 2018).

The three previously mentioned publications focussed on box-shaped twin-hull sections which are characterised by vertical side walls and sharp corners at the bilge. Moradi et al. (2015) studied different inlet configurations using a FVM with viscous flow assumptions. They found that replacing the sharp corners with rounded ones lead to significant higher resonant wave heights in the gap due to a reduction of vortex generation at the inlet. These findings rise the question if a potential flow based boundary element method can be a valid alternative to the FVM for the study of multi-hull ships with well rounded hull forms when only little influence of flow separation is expected.

The heave radiation problem of circular or semi-circular cylinder sections, which has been studied previously by several authors e.g. Ohkusu (1969), Wang and Wahab (1971), Lee et al. (1971) and Nordenstrøm et al. (1971), can be seen as a representation of such a case. A recent numerical parameter study on this case was conducted by Bonfiglio and Brizzolara (2018) using a viscous flow solver based on the FVM. They showed that the hydrodynamic coefficients as well as the wave elevation inside the gap at resonance depend nonlinearly on the heave amplitude. Their results indicate that viscosity may have an important effect at very high heave amplitudes. However, no study was found so far that quantifies the influence of viscosity on the hydrodynamic forces and shows the effects on the free surface elevation in the gap. This would be of particular interest at low to moderate motion amplitudes, which mark a typical scope of application for seakeeping analyses of multi-hull ships.

Aim of the present study was to validate the BEM/MEL approach for the case of a heaving semi-circular twin-hull section with a focus on piston mode resonance. Added mass and damping coefficients were compared to experimental results as well as results from linear theory by Wang and Wahab (1971). In order to verify the prediction quality of higher order forces, additional simulations with a FVM were conducted in the frequency range where resonant behaviour was observed. Simulations with the FVM were carried out using inviscid as well as viscous flow assumptions respectively to show the effects of viscosity. Besides the nonlinear hydrodynamic forces, the free surface elevation as well as the pressure distribution resulting from the different computational approaches were compared to each other. All simulations were carried out at a single hull distance and two different motion amplitudes.

The paper is structured as follows: At first, the geometrical properties of the problem are sketched and the applied motion is explained in conjunction with the evaluation method for the force coefficients. Next the characteristics

of the two computational methods are outlined in one section respectively, including the numerical setup and grid convergence studies. This is followed by the presentation and discussion of the results. Finally, the findings of the study are summarised in the conclusion.

2. Problem Definition

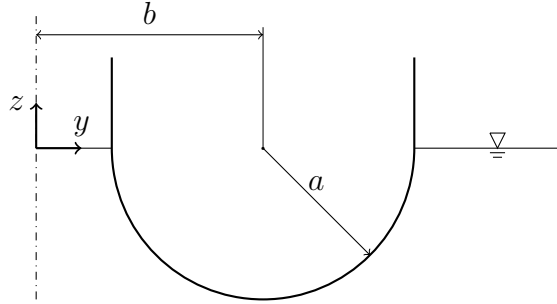


Figure 1: Sketch of the right half of the symmetric twin-hull at initial conditions including the cylinder radius a , the distance of the cylinder axes to symmetry plane b as well as the horizontal y -axis and the vertical z -axis of the coordinate system.

The examined problem is sketched in Figure 1. Two cylinders of infinite length with semi-circular cross sections of radius a and vertical walls above the circular part are considered. The cylinder axes are located in a distance $2b$ away from each other. The origin of the coordinate system is located in the symmetry plane between the cylinders on a level with the undisturbed free water surface. For the present study a hull distance of $b = 1.5a$ was chosen which corresponds to the narrowest gap size that was examined experimentally by Wang and Wahab (1971).

Initially the cylinders are floating in calm water at a draft equal to their radius, i.e. the vertical position of the cylinder axes is $z_{cyl} = 0$. At time $t = 0$ they are forced into harmonic heave oscillations with circular frequency ω :

$$z_{cyl}(t) = -z_a(t) \cdot \sin(\omega t), \quad (1)$$

$$\text{with } z_a(t) = \begin{cases} 0 & \text{if } t < 0, \\ \frac{z_A}{2} \left(\sin\left(\frac{\omega t}{2} - \frac{\pi}{2}\right) + 1 \right) & \text{if } 0 \leq t < T, \\ z_A & \text{otherwise.} \end{cases} \quad (2)$$

During the first period $T = \frac{2\pi}{\omega}$ the instantaneous motion amplitude $z_a(t)$ gradually increases according to a sine function of half the frequency until it reaches a constant value of z_A . The advantage of this formulation, opposed to a linear ramp for example, is that position, velocity and acceleration increase in a continuously differentiable way. This in turn avoids discontinuities in the hydrodynamic force.

Besides the free surface elevation in the gap, the vertical hydrodynamic force F on the body is the main subject of interest. For a comparison with the hydrodynamic mass and damping coefficients presented by Wang and Wahab (1971) extracts from the time dependent results are transformed into Fourier series using the formulation:

$$F(t) = F_0 + \sum_{k=1}^{\infty} F_k \sin(k\omega t + \psi_k). \quad (3)$$

Thus, the hydrodynamic force $F(t)$ is split up into a mean value F_0 and a sum of harmonic oscillations. The oscillations are defined as sine functions with frequency $k\omega$, amplitude F_k and phase ψ_k with k referring to an integer value which specifies the order of the respective component. Considering the definition of the motion (2), a phase angle of $\psi_1 = \pi$ means that the first order force F_1 is in phase with the displacement z_{cyl} . Thus, it acts in the opposite direction as the acceleration and behaves like an inertial force. A phase angle of $\psi_1 = \pi/2$ corresponds to a force that acts in the opposite direction as the current velocity and therefore has a damping effect. The added mass A and the damping

coefficient B can be calculated from:

$$A = \frac{-F_1 \cos(\psi_1)}{\omega^2 z_A}, \quad (4)$$

$$B = \frac{F_1 \sin(\psi_1)}{\omega z_A}. \quad (5)$$

Due to symmetry of geometry and motion it is sufficient to model only one cylinder with the computational methods and apply corresponding boundary conditions on the symmetry plane. In case that there are no shear forces, the problem described above is equivalent to a single cylinder heaving next to a vertical wall. Furthermore, the problem can be scaled to any dimension without effecting the results. For viscous simulations the same scale as in the experiments of $a = 0.1524$ m is applied.

3. Boundary Element Method

3.1. Method description

The presented boundary element method is an improved version of the potential flow solver that was used by Haase et al. (2015) in the context of 2D+t analyses of planning hulls and is based on the approach presented by Greco (2001) and Sun (2007). More recently it was applied by Simonis et al. (2020) in a 2D+t based seakeeping analysis of a semi-displacement hull. In the following, the method's basic features are outlined.

In the context of potential theory the flow is assumed to be incompressible and irrotational. As a consequence, viscosity is neglected and the velocity field \mathbf{q} may be expressed as the gradient of a potential ϕ :

$$\mathbf{q} = \nabla \phi \quad (6)$$

Conservation of mass for an incompressible fluid leads to the Laplace equation, which in the case of a two dimensional domain can be written as:

$$\frac{\partial^2 \phi}{\partial y^2} + \frac{\partial^2 \phi}{\partial z^2} = 0. \quad (7)$$

Based on Green's second identity a generalised solution of the Laplace equation for a point $\mathbf{x}(y, z)$ inside the fluid domain can be found in terms of the values for ϕ and $\frac{\partial \phi}{\partial n}$ on the boundary S of the domain:

$$\alpha(\mathbf{x})\phi(\mathbf{x}) = \int_S \left(\phi \frac{\partial}{\partial n} \ln r - \frac{\partial \phi}{\partial n} \ln r \right) dS \quad (8)$$

The angle α describes the angular extent of an arc which has an infinitesimal radius, it's center at the position of \mathbf{x} and is entirely within the fluid domain, i.e. it is $\alpha = 2\pi$ if \mathbf{x} is located fully inside the fluid domain and $\alpha = \pi$ if \mathbf{x} lies on a sufficiently smooth boundary. The expression $\partial/\partial n$ denotes a derivative in the direction of the two-dimensional normal vector $n_y \mathbf{j} + n_z \mathbf{k}$ on the boundary. The distance between the point \mathbf{x} and a point on the boundary is referred to as r .

The boundary is subdivided in several parts: The free surface, which is described by the coordinates y_{FS} and z_{FS} , the body, the symmetry plane and the outer boundaries. Following conditions are imposed on the respective boundaries:

$$\frac{D\phi}{Dt} = \frac{1}{2} \left(\frac{\partial \phi}{\partial y} \right)^2 + \frac{1}{2} \left(\frac{\partial \phi}{\partial z} \right)^2 - g z_{FS}, \quad (9)$$

$$\frac{Dy_{FS}}{Dt} = \frac{\partial \phi}{\partial y}, \quad \frac{Dz_{FS}}{Dt} = \frac{\partial \phi}{\partial z} \quad (10)$$

at the free surface with g referring to the gravitational acceleration,

$$\frac{\partial \phi}{\partial n} = \frac{\partial z_{cyl}}{\partial t} n_z \quad (11)$$

on the hull and

$$\frac{\partial \phi}{\partial n} = 0 \quad (12)$$

on the symmetry plane and on the outer boundaries.

The free surface boundary conditions (9) and (10) are used to compute the development of the free surface shape as well as the value for ϕ on the free surface in time via numerical integration. The required values on the right hand side of the equations are obtained by numerically solving a boundary value problem with respect to ϕ using a discretised version of the integral equation (8). For this purpose, as well as for tracking the free surface shape in time, the domain boundary is divided into a finite number of straight-line elements.

The instantaneous values for ϕ are imposed at the nodes of the free surface elements whereas $\partial \phi / \partial n$ is prescribed at the nodes of the other elements. A linear distribution of ϕ and $\partial \phi / \partial n$ is assumed inbetween the nodes of each element. The solution of the integration according to equation (8) over such an element is known analytically in terms of the nodal values (see e.g. Greco (2001)). Thus, equation (8) can be expressed as the sum of the known solutions for all elements. Formulating such a discretised integral equation for each node respectively yields an equations system that is used to determine the unknown nodal values.

Subsequently, the velocities $\partial \phi / \partial x$ and $\partial \phi / \partial y$, which are needed to evaluate the right hand sides of equations (9) and (10), can be computed. The free surface boundary conditions are integrated with respect to time using a fourth order Runge-Kutta scheme. A new free surface shape is obtained by moving the free surface nodes accordingly. Regridding algorithms are applied to compensate for numerical inaccuracies and increase the robustness of the method.

As the boundary conditions are not linearised with respect to the potential ϕ and evaluated at the actual instantaneous position of the free surface and the hull, large deformations of the free surface can be simulated. Because equations (9) and (10) are substantial time derivatives, the nodes on the free surface are considered as fluid particles in the solution process described above. Since the boundary value problem for ϕ is solved in the Eulerian frame and the free surface is treated in a Lagrangian sense at the same time, the procedure is called MEL-approach (mixed Eulerian Lagrangian) and was used by Longuet-Higgins and Cokelet (1976) for the first time to predict the shape of steep water waves.

The pressure p on the hull surface is calculated using the Bernoulli equation for unsteady potential flow

$$p - p_0 = -\rho \left(\frac{\partial \phi}{\partial t} + \frac{1}{2} \left(\frac{\partial \phi}{\partial y} \right)^2 + \frac{1}{2} \left(\frac{\partial \phi}{\partial z} \right)^2 + gz \right), \quad (13)$$

with ρ referring to the fluid density and p_0 to the reference pressure at $z = 0$ when the fluid is at rest. The dynamic pressure p_d is obtained by excluding the hydrostatic pressure ρgz :

$$p_d = p - p_0 + \rho gz. \quad (14)$$

The dynamic force F in equation (3) is obtained by integrating the dynamic pressure over the body surface. The local time derivative of the potential at a grid node with velocity $\dot{\mathbf{x}}_p$ is computed from

$$\frac{\partial \phi}{\partial t} = \frac{d\phi}{dt} - \dot{\mathbf{x}}_p \cdot \nabla \phi, \quad (15)$$

where the total time derivative $d\phi/dt$ is approximated from the potential at the current and at the last time step with finite differences.

In order to avoid reflections of the radiated waves from the outer boundary, a numerical damping zone is introduced by modifying the dynamic free surface boundary condition inbetween a position y_{dmp} and the boundary at y_{bnd} :

$$\frac{D\phi}{Dt} = \frac{1}{2} \left(\frac{\partial \phi}{\partial y} \right)^2 + \frac{1}{2} \left(\frac{\partial \phi}{\partial z} \right)^2 - gz - \delta(y) \frac{\partial \phi}{\partial n}. \quad (16)$$

The absorption coefficient δ is gradually increased over the distance l_{rmp} and then kept constant:

$$\delta(y) = \begin{cases} 0 & \text{for } y \leq y_{dmp}, \\ \delta_0 \left(-2 \left(\frac{y - y_{dmp}}{l_{rmp}} \right)^3 + 3 \left(\frac{y - y_{dmp}}{l_{rmp}} \right)^2 \right) & \text{for } y_{dmp} < y \leq y_{dmp} + l_{rmp}, \\ \delta_0 & \text{for } y_{dmp} + l_{rmp} < y. \end{cases} \quad (17)$$

Table 1

 Parameters used for the automated grid generation for the BEM and their dependency on the radiated wavelength λ .

Parameter	Expression	Meaning
$s_{bdy,max}$	$\frac{\pi a}{60}$	Maximum element size on the body
s_{fs}	$\frac{\lambda}{60}$	Target element size on the free surface
$s_{fs,max}$	$\frac{\lambda}{10}$	Maximum element size on the free surface
y_{dmp}	$3\lambda + a + b$	Y-coordinate of start of damping zone (see (17))
l_{rmp}	2λ	Length over which the absorption factor is increased (see (17))
y_{bnd}	$100\lambda + a + b$	Y-coordinate of right boundary
z_{bnd}	$100\lambda + 2a$	Z-coordinate of lower boundary

Following the recommendation of Sun (2007) a value of $\delta_0 = 0.3\sqrt{ga}$ is chosen. The values for y_{dmp} , y_{bnd} and l_{rmp} are given in Table 1 in terms of the radiated wavelength λ and further explained in the following section.

3.2. Numerical setup

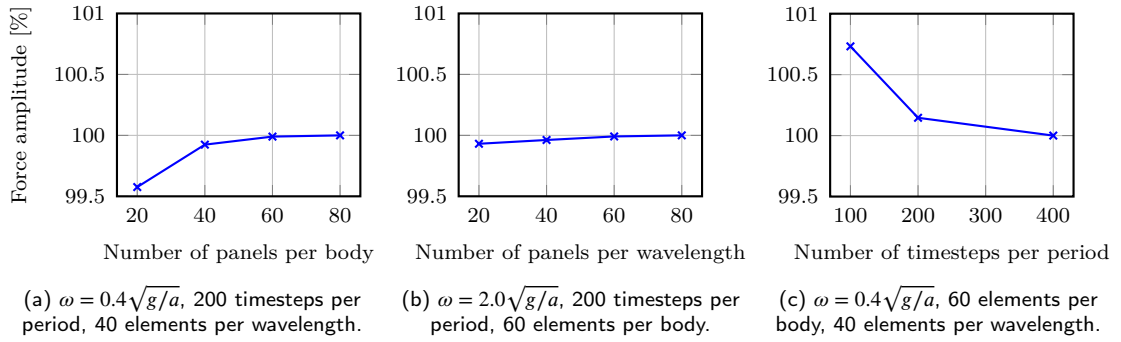


Figure 2: Dynamic force amplitudes of single heaving cylinders calculated with the BEM at different mesh configurations. Results are related to the amplitude of the finest discretisation within each plot.

As indicated in section 3.1 only the domain boundaries need to be discretised for the BEM. The grid resolution required on the free surface as well as the positions of the right and lower domain boundaries and the damping zone mainly depend on the radiated wave length. Since a broad range of oscillation frequencies shall be considered, an automated grid generation process has been established that uses the radiated wave length λ as a scale. The wave length is calculated from the oscillation frequency with the dispersion relation for deep water:

$$\lambda = \frac{2\pi g}{\omega^2}. \quad (18)$$

The parameters used to determine the grid generation process are summarised in Table 1. All parameters except of $s_{bdy,max}$ are expressed in terms of the wave length. The discretisation process distinguishes between low frequency cases ($s_{bdy,max} \leq s_{fs}$) and high frequency cases ($s_{bdy,max} > s_{fs}$). In low frequency cases the element size on the body is determined by $s_{bdy,max}$. On the free surface the same element size is kept in the vicinity of the body up to a distance equal to the gap size. From there, the element size gradually increases with the distance from the body. The growth factor is defined such that the element size reaches $s_{fs,max}$ when the damping factor has reached its maximum ($y = y_{dmp} + l_{rmp}$). The same growth factor is kept up to the right boundary which leads to very large element sizes and allows for a large domain size. Reflections, which would normally occur if the element size grows too large, are suppressed by the damping zone.

In high frequency cases the element size on the body is determined by s_{fs} . On the free surface the same element size is kept up to the border of the damping zone at y_{dmp} . Then, the element size is increased in the same manner as in

low frequency cases. The reason for the distinction in low and high frequency cases is the need to maintain a similar element size on the body and the free surface next to it. For low frequencies the element size determined from $s_{fs,max}$ becomes too large for a proper discretisation of the body geometry. At higher frequencies however, the element size determined by $s_{bdy,max}$ is too large to capture the flow details.

Convergence studies regarding the spatial and temporal discretisation were carried out on the basis of heave simulations of a single cylinder. These studies were used to define the expressions indicated in Table 1. Exemplary results for the behaviour of the force amplitudes using different mesh configurations are presented in Figure 2.

Following the explanations above, the maximum element size on the body $s_{bdy,max} = \pi a/60$ was chosen on the basis of a low frequency case. Although a target element size on the free surface of $s_{fs} = \lambda/40$ seems sufficiently accurate for the single cylinder at high frequency oscillations, the value was decreased to $s_{fs} = \lambda/60$ in order to account for the strong fluid motion in case of piston-mode resonance. To avoid any influence from the lower and right boundary, they were located at large distances of about 100λ away from the body. These large domain sizes become affordable due to the growth of the element sizes with increasing distance from the body. The temporal discretisation was set to 200 timesteps per period when the motion amplitude was $z_A = a/24$. When the motion amplitude was $z_A = a/12$, 800 timesteps per period were used to account for the higher flow velocities in the gap and ensure numerical stability.

4. Finite Volume Method

4.1. Method description

For the presented study the commercial simulation software Star-CCM+ was used. The software incorporates a finite volume method to solve for pressure and velocities in a given fluid domain. Free surface effects can be captured by means of the volume of fluid technique. The fundamental characteristics of the approach are outlined in the following.

The finite volume method requires a subdivision of the whole fluid domain into several discrete control volumes (cells). Conservation equations are formulated for each control volume in integral form. The values of interest are stored at the cell centres or the cell faces and as each equation depends on the nodal values of neighbouring cells, a solvable equation system is formed.

For the problem at hand incompressible flow is assumed. The governing equations are the conservation of mass

$$\nabla \cdot \mathbf{q} = 0 \quad (19)$$

and momentum

$$\rho \left(\frac{\partial \mathbf{q}}{\partial t} + \mathbf{q} \cdot \nabla \mathbf{q} \right) = -\nabla \rho g z - \nabla p + \mu \nabla^2 \mathbf{q}. \quad (20)$$

For the viscous simulations a laminar boundary layer is assumed. If inviscid flow assumptions are made, the viscosity μ is set equal to zero. A segregated flow model is invoked which solves for pressure and velocity by linking the momentum and continuity equations with a predictor corrector approach. This involves a colocated variable arrangement and an implicit unsteady solution scheme.

Both phases, water and air, are included in the fluid domain and the free surface is captured using the volume of fluid technique. This means that the local material properties (ρ, μ) are treated as a blend of the values for water (ρ_w, μ_w) and air (ρ_a, μ_a) and are expressed in terms of the volume fraction of water c :

$$\rho = c\rho_w + (1 - c)\rho_a, \quad (21)$$

$$\mu = c\mu_w + (1 - c)\mu_a. \quad (22)$$

The volume fraction on the other hand is determined by solving an additional transport equation:

$$\frac{\partial c}{\partial t} + \nabla \cdot (c\mathbf{q}) = 0. \quad (23)$$

The dynamic pressure p_d is obtained from the pressure p by subtracting the hydrostatic pressure as specified in equation (14). The dynamic force F in equation (3) is calculated by integrating p_d over the wetted part of the body surface and adding the shear forces in case viscous flow assumption were made.

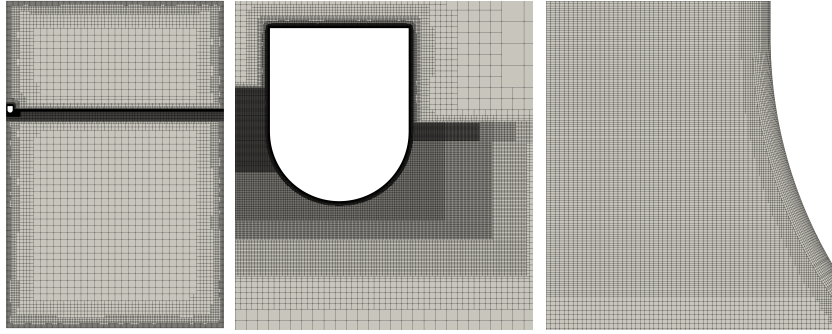


Figure 3: Overview of the mesh used for the FVM simulations (left) and details of the refinements around the body (middle) and in the gap (right).

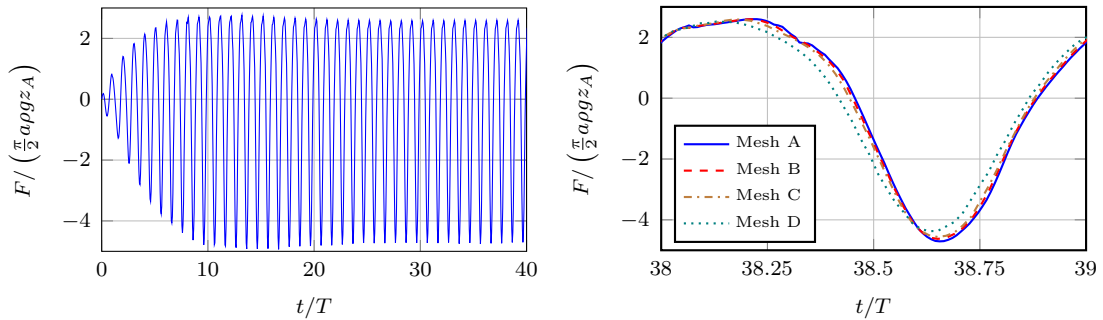


Figure 4: Time history of dynamic heave force at $\omega = 0.82\sqrt{g/a}$ calculated with FVM using inviscid flow assumptions and mesh A (left) and comparison of dynamic heave force over one period using different mesh configurations (right)

4.2. Numerical setup

An unstructured mesh was used for the finite volume simulations consisting mainly of hexahedral cells. Local refinements were applied in vicinity of the free surface, the body and in the gap (see Figure 3). To account for the two-dimensional flow, only one layer of cells was used with respect to the x-direction and symmetry conditions were imposed to the forward and backward boundary. Velocity inlet conditions were applied at the upper and lower boundary. As in the potential flow simulations a symmetry condition was used on the left boundary. On the right a pressure outlet condition was employed. Additionally, a damping zone was defined starting at a distance of $20a$ from the right boundary. The total extent of the domain was $81.92a$ in y-direction and in z-direction underneath the undisturbed free surface. Above the free surface it was $40.96a$. The heave motion (2) was applied to the whole grid.

Four meshes with different numbers of cells were generated and convergence of the hydrodynamic force was checked on the basis of inviscid simulations at piston mode resonance ($\omega = 0.82\sqrt{g/a}$) with a motion amplitude of $z_A = a/24$. The meshing algorithm is controlled via a base size parameter, which corresponds to the target edge length of the cells around the body. The value was $a/200$ for mesh configuration A and was consecutively doubled up to $a/25$ for mesh D. The overall cell counts were 137,433 for mesh A, 41,417 for mesh B, 16,537 for mesh C and 8,388 for mesh D. The number of time steps per period were 4,000 for mesh A, 2,000 for mesh B, 1,000 for mesh C and 500 for mesh D. An illustration of mesh A and the refinements next to the body can be found in Figure 3. It should be noted that the grid was not fully optimised and the number of cells could possibly be further reduced without effecting the quality of the results.

On the left hand side of Figure 4 the time history of the hydrodynamic force calculated with mesh configuration A is shown. It is evident that the force amplitude reaches a nearly constant value after approximately 30 periods. The right hand side of Figure 4 shows a comparison of the results for the vertical hydrodynamic force using the different meshes. It is noted that the forces obtained with mesh C already agree fairly well with the results from the finest mesh A, while the coarsest mesh D is clearly inappropriate. By comparison of the flow fields it was observed that some details of the flow, e.g. breaking waves, could not be captured with the coarser meshes. Therefore, mesh A was

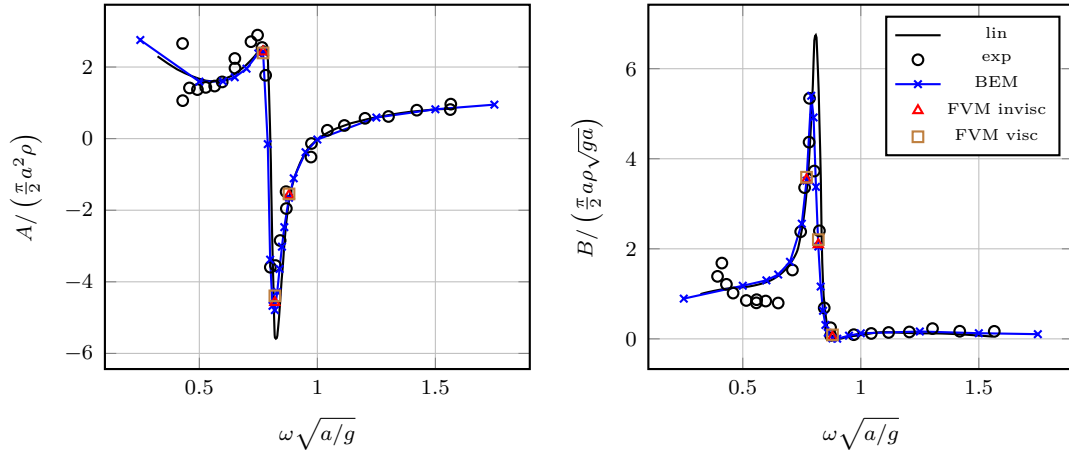


Figure 5: Hydrodynamic mass (left) and damping coefficients (right) determined from the dynamic force calculated with BEM, FVM using inviscid flow assumptions (FVM invisc) and FVM using viscous flow assumptions (FVM visc) with $z_A = a/24$ compared to experimental (exp) as well as theoretical (lin) results by Wang and Wahab (1971).

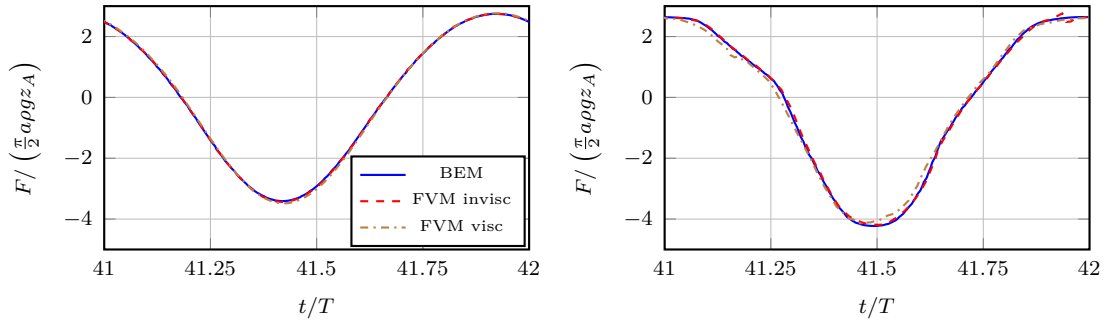


Figure 6: Time history of dynamic heave force over one period calculated with BEM, FVM using inviscid flow assumptions (FVM invisc) and FVM using viscous flow assumptions (FVM visc) with $\omega = 0.77\sqrt{g/a}$, $z_A = a/24$ (left) and $z_A = a/12$ (right).

chosen for all further studies with motion amplitude $z_A = a/24$. A slightly modified version with increased height of the refinement zone in the gap was used for the simulations with $z_A = a/12$ to account for the higher free surface elevation amplitudes.

5. Results and Discussion

All simulations were carried out for the motion amplitudes $z_A = a/24$ and $z_A = a/12$, a hull distance of $b = 1.5a$ and lasted over 51 periods. A total of 18 frequencies from $\omega = 0.25\sqrt{g/a}$ to $\omega = 1.75\sqrt{g/a}$ was examined with the BEM. Additionally, the frequencies $\omega = 0.77\sqrt{g/a}$, $\omega = 0.82\sqrt{g/a}$ and $\omega = 0.88\sqrt{g/a}$ were simulated with the FVM using viscous and inviscid flow assumptions respectively. For each simulation, the resulting hydrodynamic heave force $F(t)$ inbetween $t/T = 40.25$ and $t/T = 50.25$ was transformed into a Fourier series as specified in equation (3). First order Fourier coefficients were compared to experimental data and linear theory in form of hydrodynamic mass and damping. Detailed comparison between the respective simulation approaches were based on the first three orders of Fourier coefficients. Additionally, the free surface elevation at characteristic time instants and respective pressure distributions on the body were taken into account to discuss deviations between the numerical approaches.

The comparison of hydrodynamic mass and damping coefficients with experimental and theoretical results from Wang and Wahab (1971) is given in Figure 5. The motion amplitude in the simulations was $z_A = a/24$ which is the same value as in the experiments. The strong variation of the hydrodynamic coefficients around $\omega \approx 0.8\sqrt{g/a}$

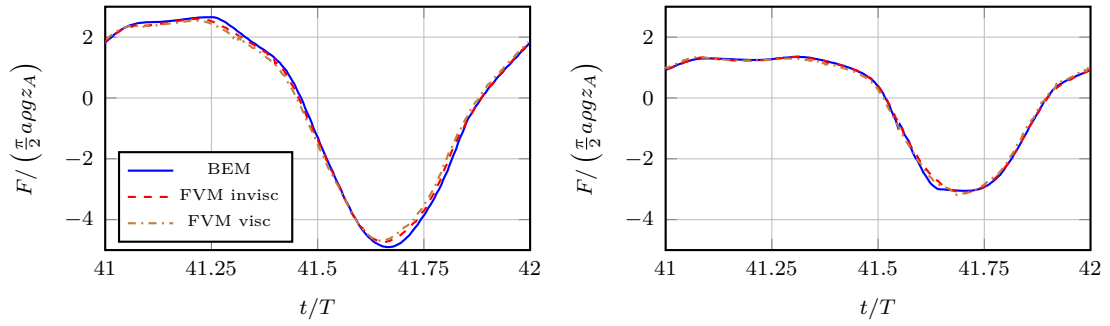


Figure 7: Time history of dynamic heave force over one period calculated with BEM, FVM using inviscid flow assumptions (FVM invisc) and FVM using viscous flow assumptions (FVM visc) with $\omega = 0.82\sqrt{g/a}$, $z_A = a/24$ (left) and $z_A = a/12$ (right).

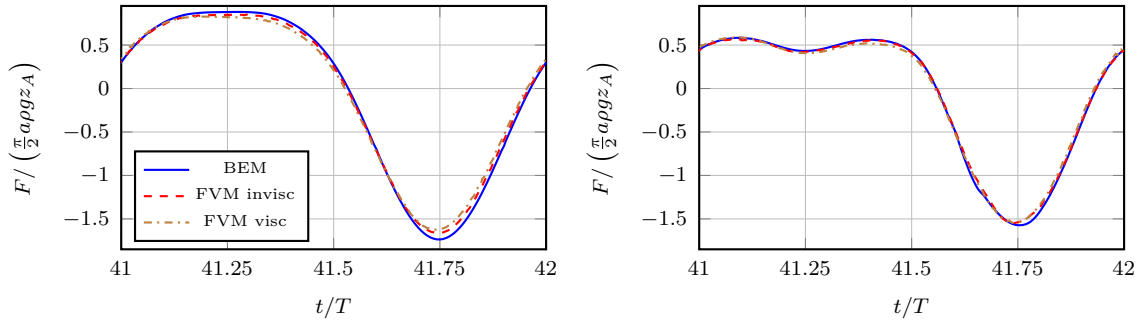


Figure 8: Time history of dynamic heave force over one period calculated with BEM, FVM using inviscid flow assumptions (FVM invisc) and FVM using viscous flow assumptions (FVM visc) with $\omega = 0.88\sqrt{g/a}$, $z_A = a/24$ (left) and $z_A = a/12$ (right).

corresponds to the piston mode resonance phenomena. Very good agreement between the nonlinear computations and the experimental results is found in that area, whereas the linear method seems to overpredict the peak values. At frequencies without resonant fluid motion the BEM results agree very well with linear theory. Deviations from the experimental values occur at lower frequencies. The experimental results show a strong scattering in that range, which according to Wang and Wahab (1971) could be due to structural oscillations of the end boards.

The cases that were simulated with the FVM represent characteristic marks with regard to the variation of added mass and damping in Figure 5. The added mass coefficient becomes rapidly negative inbetween $\omega = 0.77\sqrt{g/a}$ and $\omega = 0.82\sqrt{g/a}$, while the latter marks the minimum value at the same time. The damping coefficient reaches zero at $\omega \approx 0.88\sqrt{g/a}$. Figures 6 - 8 illustrate time histories of the dynamic heave force at these frequencies over one period for $z_A = a/24$ and $z_A = a/12$ respectively. Except for the case with $\omega = 0.77\sqrt{g/a}$ and $z_A = a/24$, all results visibly deviate from the sinusoidal course of the motion excitation. This nonlinear tendency is further stressed when comparing the results corresponding to the lower motion amplitude to the respective curves corresponding to the higher motion amplitude.

The agreement between the numerical approaches is generally very good. Visible differences can be identified for $z_A = a/24$ at $\omega = 0.82\sqrt{g/a}$ and $\omega = 0.88\sqrt{g/a}$ around the peak values which are somewhat overpredicted by the BEM compared to both FVM approaches. A visible influence of viscosity can be identified at $\omega = 0.77\sqrt{g/a}$ and $z_A = a/12$. The curves of BEM and inviscid FVM are very close together in that case, while the curve from the viscous FVM shows a small deviation.

A comparison of the Fourier coefficients derived from the respective time histories of the dynamic force at $z_A = a/24$ is shown in Figure 9 up to order $k = 3$. All results agree well and show the same trends with regard to frequency. The first order force amplitude F_1 increases slightly from $\omega = 0.77\sqrt{g/a}$ to $\omega = 0.82\sqrt{g/a}$ and then decreases again

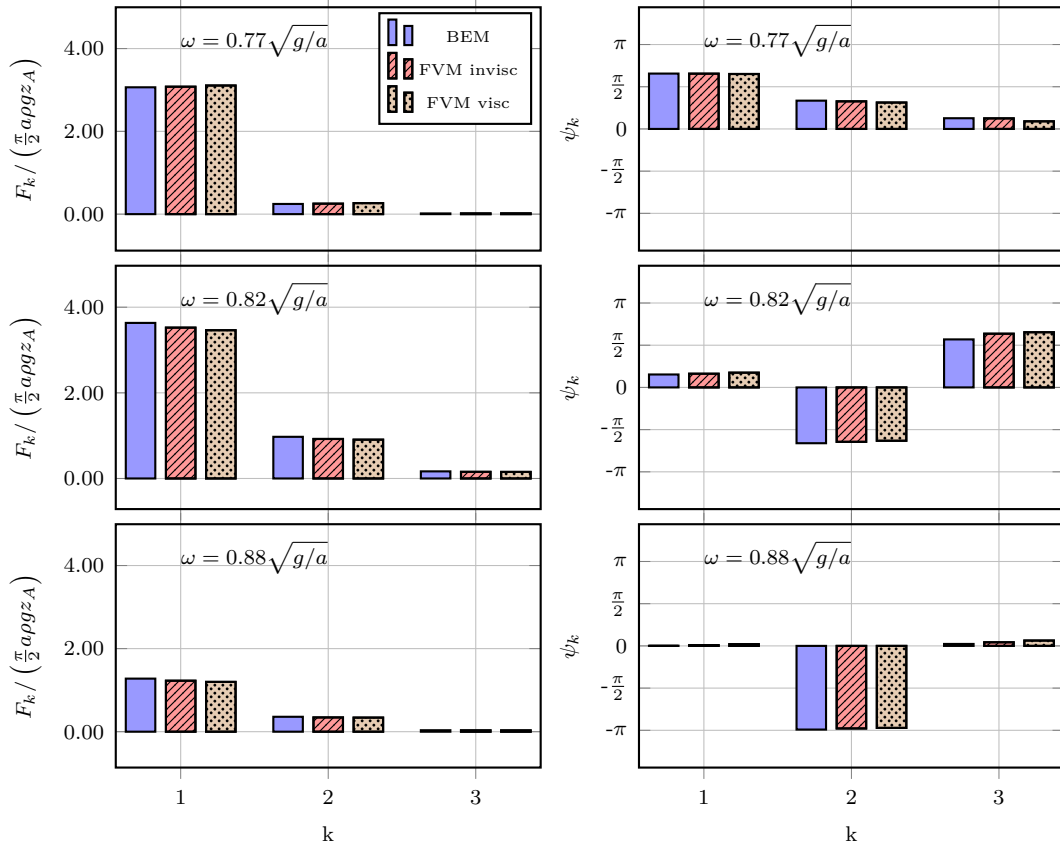


Figure 9: Force amplitudes F_k (left) and corresponding phase angles ψ_k (right) of different order k derived via Fourier analysis of dynamic force calculated with BEM, FVM using inviscid flow assumptions (FVM invisc) and FVM using viscous flow assumptions (FVM visc) with $z_A = a/24$.

towards $\omega = 0.88\sqrt{g/a}$. By looking at the corresponding phase angle, the variation of added mass and damping coefficients over frequency (Figure 5) can be retraced: At $\omega = 0.77\sqrt{g/a}$ the first order phase angle ψ_1 is between π and $\pi/2$ which, according to equation (4), means a positive added mass coefficient. On the contrary, the phase angle is between zero and $\pi/2$ at $\omega = 0.82\sqrt{g/a}$ which leads to a negative added mass coefficient. At $\omega = 0.88\sqrt{g/a}$ it becomes almost zero which, according to equation (5), means that the damping coefficient is almost zero as well.

Amongst the cases shown in Figure 9, the second order force amplitudes are highest at $\omega = 0.82\sqrt{g/a}$. However, the relative contribution of the second order force to the overall force is the highest at $\omega = 0.88\sqrt{g/a}$. It is interesting to note that the second order phase angle shows an even stronger variation with frequency than the first order phase angle. Contributions of the third order force are highest at $\omega = 0.82\sqrt{g/a}$ but rather small at all three sample frequencies.

The Fourier coefficients corresponding to the motion amplitude $z_A = a/12$ are presented in Figure 10. By comparison with the results corresponding to $z_A = a/24$ in Figure 9, a very pronounced difference can be found regarding the first order force amplitudes: At $\omega = 0.82\sqrt{g/a}$ the nondimensional value is significantly lower at the larger motion amplitude, while at $\omega = 0.77\sqrt{g/a}$ it is higher. This further demonstrates the nonlinear relationship between body motion and the forces, as doubling the motion amplitude does not result in twice the force amplitude, i.e. a constant nondimensional value. Additionally, the significance of second order force components seems to increase with motion amplitude. A factor that might influence the behaviour of force coefficients observed here is a dependence of the resonance frequency on the motion amplitude, which was also found by Bonfiglio and Brizzolara (2018).

The presented time histories of the dynamic forces and the corresponding Fourier coefficients demonstrate that the three numerical approaches are all able to resolve the nonlinear characteristics of the heave radiation problem and only minor differences between the methods can be taken from the respective plots. In order to analyse these differences in

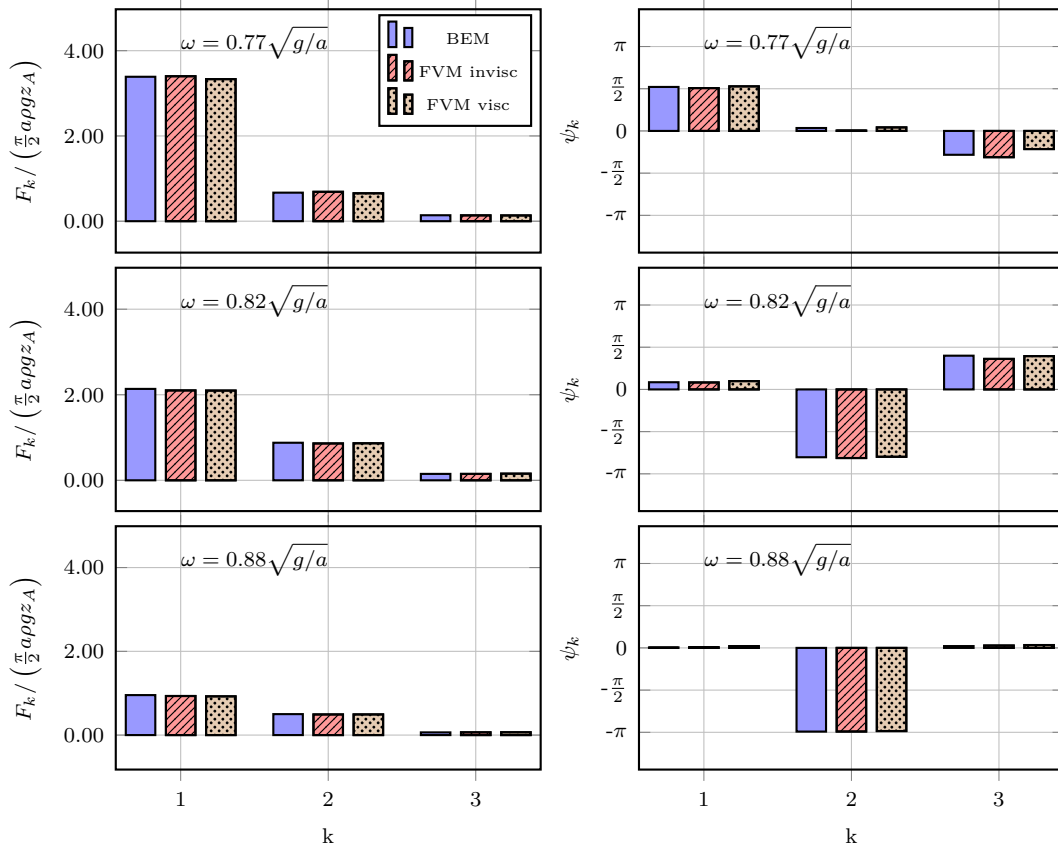


Figure 10: Force amplitudes F_k (left) and corresponding phase angles ψ_k (right) of different order k derived via Fourier analysis of dynamic force calculated with BEM, FVM using inviscid flow assumptions (FVM invisc) and FVM using viscous flow assumptions (FVM visc) with $z_A = a/12$.

detail, the force components resulting from the viscous FVM were subtracted from the respective results of inviscid FVM as well as BEM. The differences were related to the total values from the viscous FVM and are given in Table 2 for $z_A = a/24$ and in Table 3 for $z_A = a/12$.

Considering that the assumptions on fluid viscosity was the only difference between the numerical setups of the two finite volume based approaches, the values in the columns titled *FVM invisc* are taken as a quantitative measure of the influence of viscosity on the force amplitudes. Amongst the analysed cases, the highest value can be found at $\omega = 0.77\sqrt{g/a}$ and $z_A = a/24$ for the third order force component. However, it should be noted that the absolute value of that force component is close to zero. Thus, it's contribution to the overall force is very small (see Figure 9). Regarding the second order force components, a notable influence of viscosity of about 5.3% can be found at $\omega = 0.77\sqrt{g/a}$ and $z_A = a/12$. The influence of viscosity on the first order force component, which arguably has the largest impact on the overall force, is below 2.4% amongst all cases.

The force amplitudes from the BEM tend to deviate more from the viscous results than the ones from the inviscid FVM, while the agreement generally seems to be better at the higher motion amplitude. To further evaluate possible reason for the deviations, the free surface elevation is considered in the following.

Figures 11 and 12 show the free surface elevation in the gap at four characteristic time instants for each of the sample frequencies. The time instant $t = 41.00T$ corresponds to a motion state with $z_{cyl} = 0$, negative velocity and zero acceleration of the body (see equation (2)). At $t = 41.25T$ the body has reached it's minimum position $z_{cyl} = -z_A$ with zero velocity and positive acceleration. Accordingly, $t = 41.5T$ means $z_{cyl} = 0$, positive velocity and zero acceleration and $t = 41.75T$ refers to the maximum position $z_{cyl} = z_A$, zero velocity and negative acceleration.

From the plots it is evident that all numerical approaches predict a phase shift between the fluid motion and the

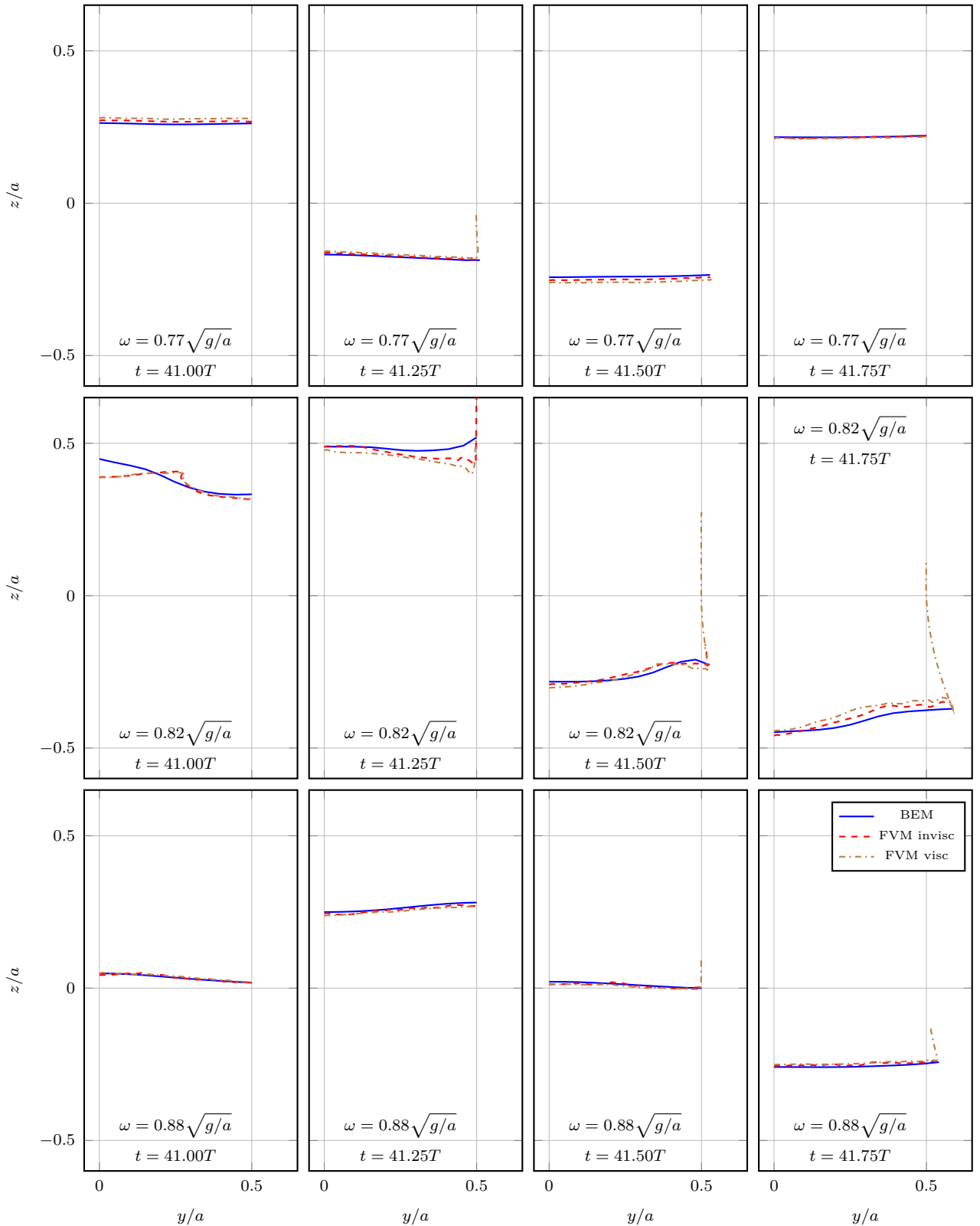


Figure 11: Instantaneous free surface elevation between the symmetry plane and the body at four time instants calculated with BEM, FVM using inviscid flow assumptions (FVM invisc) and FVM using viscous flow assumptions (FVM visc) with $z_A = a/24$ for each of the three sample frequencies.

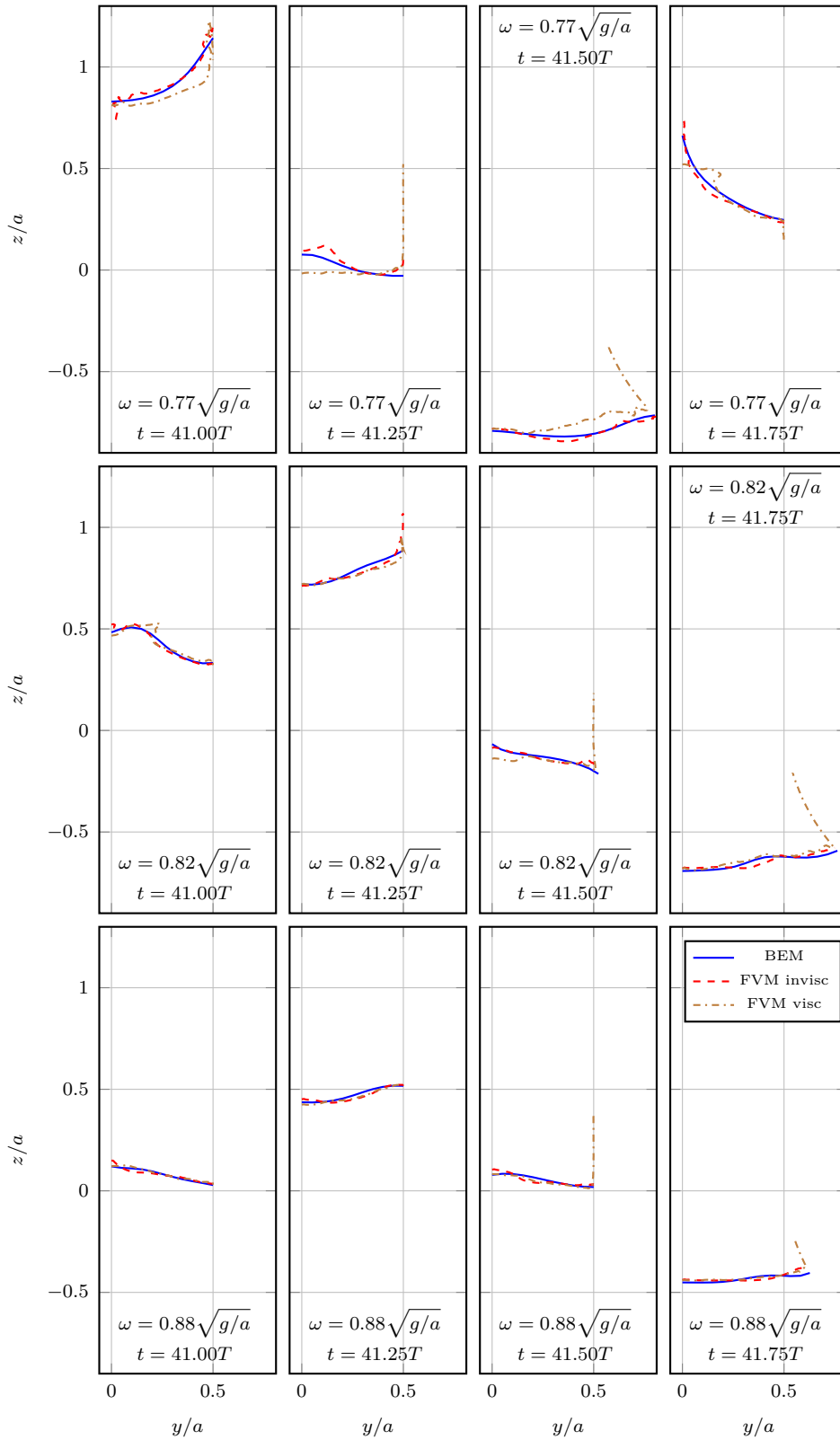


Figure 12: Instantaneous free surface elevation between the symmetry plane and the body at four time instants calculated with BEM, FVM using inviscid flow assumptions (FVM invisc) and FVM using viscous flow assumptions (FVM visc) with $z_A = a/12$ for each of the three sample frequencies.

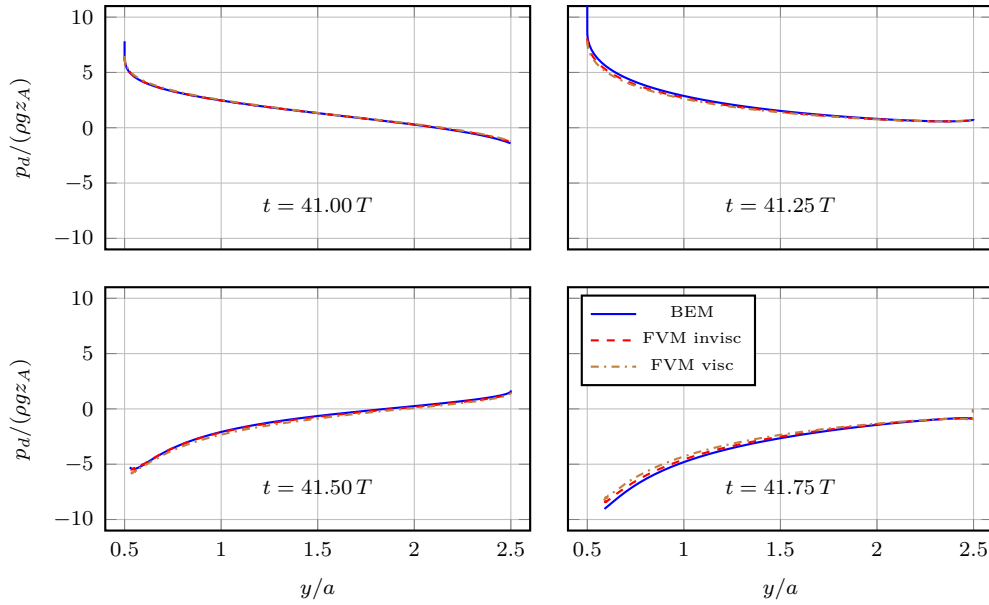


Figure 13: Instantaneous dynamic pressure distribution on the body at four time instants calculated with BEM, FVM using inviscid flow assumptions (FVM invisc) and FVM using viscous flow assumptions (FVM visc) with $z_A = a/24$ and $\omega = 0.82\sqrt{g/a}$.

Table 2

Relative deviations ΔF_k of force amplitudes calculated using inviscid flow assumptions (FVM invisc, BEM) compared to force amplitudes calculated using viscous flow assumptions at $z_A = a/24$ with k denoting the order of the respective amplitude.

$\omega\sqrt{a/g}$	ΔF_1 [%]		ΔF_2 [%]		ΔF_3 [%]	
	FVM invisc	BEM	FVM invisc	BEM	FVM invisc	BEM
0.77	-0.92	-1.38	-4.70	-7.49	-9.56	-10.29
0.82	1.75	4.93	1.79	7.33	1.08	8.32
0.88	2.36	6.57	1.17	5.77	1.41	11.22

Table 3

Relative deviations ΔF_k of force amplitudes calculated using inviscid flow assumptions (FVM invisc, BEM) compared to force amplitudes calculated using viscous flow assumptions at $z_A = a/24$ with k denoting the order of the respective amplitude.

$\omega\sqrt{a/g}$	ΔF_1 [%]		ΔF_2 [%]		ΔF_3 [%]	
	FVM invisc	BEM	FVM invisc	BEM	FVM invisc	BEM
0.77	2.04	2.85	5.24	5.88	1.31	4.39
0.82	0.17	2.17	-0.45	1.71	-4.01	-2.28
0.88	0.89	3.88	-0.15	1.75	-1.95	-3.86

body motion which depends on frequency. Such a dependence is in line with experimental findings on moonpools (Faltinsen et al., 2007). As was shown before in Figures 9 and 10, the phase angles of the force components also depend on frequency and the strong variation of hydrodynamic coefficients (Figure 5) can be retraced to the variation of the first order phase angle using equation (4). As the free surface elevation might be seen as an indication of the pressure inside the gap, which influences the forces on the body, it is suspected that the phase shift of the forces is caused by the phase shift of the fluid motion inside of the gap. This would lead to the conclusion that the phase shift of the fluid motion is a reason for the strong variation of the hydrodynamic mass and damping coefficients. Such an explanation would fit well to the statements made by Lewandowski (1992) on the matter.

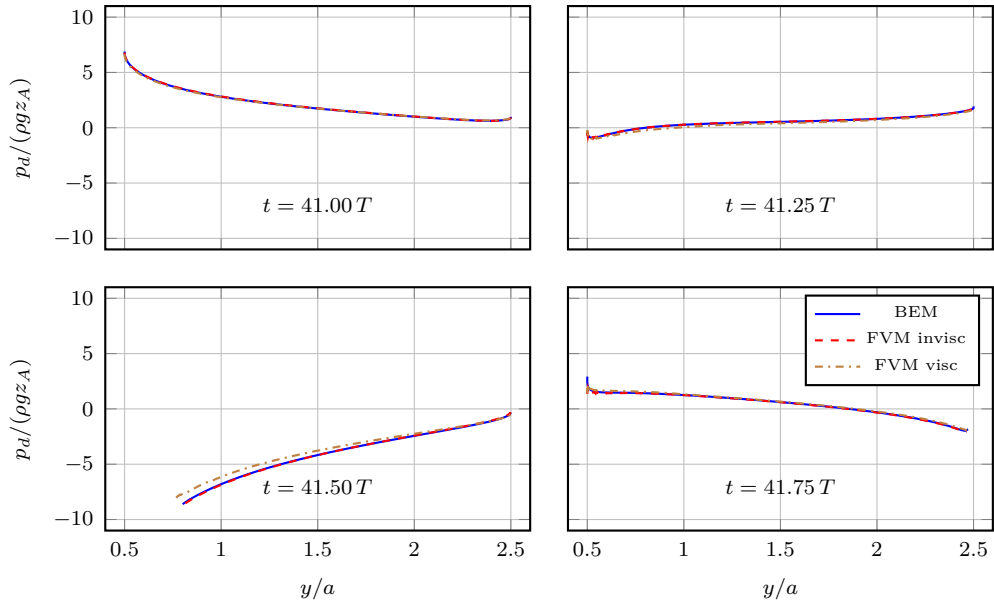


Figure 14: Instantaneous dynamic pressure distribution on the body at four time instants calculated with BEM, FVM using inviscid flow assumptions (FVM invisc) and FVM using viscous flow assumptions (FVM visc) with $z_A = a/12$ and $\omega = 0.77\sqrt{g/a}$.

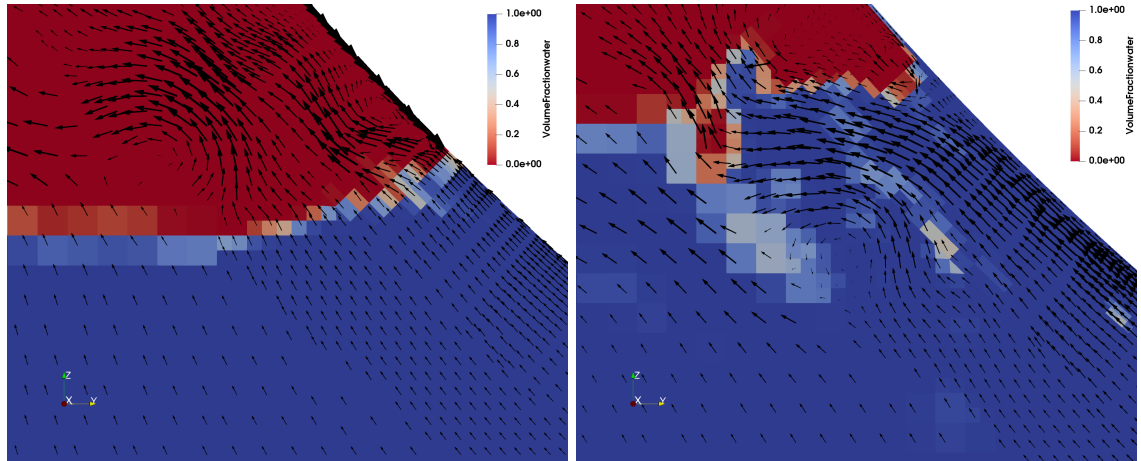


Figure 15: Instantaneous volume fraction (coloured) and flow velocity relative to the body motion (arrows) resulting from the FVM with inviscid (left) and viscous (right) flow assumptions at $t = 41.50 T$, $\omega = 0.77\sqrt{g/a}$ and $z_A = a/12$.

The overall free surface level predicted by the different numerical approaches agrees very well in most cases. For the motion amplitude of $z_A = a/24$ (Figure 11), the best agreement is found at $\omega = 0.77\sqrt{g/a}$ and $\omega = 0.88\sqrt{g/a}$ where, as the term piston-mode resonance implies, the free surface is nearly flat and varies its level in time. At $\omega = 0.82\sqrt{g/a}$ the level difference over one period is largest and the free surface is not entirely flat anymore. A possible reason for this behaviour is that lateral velocities are induced when the free surface moves to a large extent along the cylindrical part of the body, effectively widening the gap width. Notable differences regarding exact free surface shape predicted by BEM and FVM are present at this frequency.

In order to evaluate how these differences might be connected to the deviation of force amplitudes (Table 2), the dynamic pressure distribution on the body at the respective timesteps is given in Figure 13. It can be taken that the different shapes at $t = 41.00 T$ have no visible effect on the pressure distribution. However, when the differences of free

surface elevation are located closer to body at $t = 41.25 T$, slight differences are evident in the pressure distribution as well. This time instant roughly corresponds to the maximum dynamic force as shown on the left side of Figure 8. The most significant difference in the pressure distribution can be found at $t = 40.75 T$. Here, the differences between the free surface shapes is not larger than before but they occur on a level with the cylindrical part of the body. This time instant is close to the minimum of the force which also marks the point in time where deviations between BEM and FVM are largest (Figure 8, left).

Based on these findings, different predictions of the free surface shape are suspected to be the main cause for deviations between BEM and FVM at $z_A = a/24$. A possible reason could be the much finer resolution of the free surface in the FVM. Additionally, the regridding algorithms used with the BEM have a filtering effect and could blur certain details of the free surface shape. As the influence of these techniques on the free surface shape is relatively higher when the overall free surface amplitude is low, it may also give an explanation why the relative agreement between BEM and FVM is better at higher motion amplitude (see Tables 2 and 3).

From Figure 12 it can be taken that the amplitude of fluid motion in the gap is considerably higher at $z_A = a/12$. An interesting case regarding the influence of viscosity is found at $\omega = 0.77\sqrt{g/a}$. Both inviscid approaches show a very good agreement here, while the results from the viscous FVM deviate. The respective dynamic pressure distribution on the body for this case is shown in Figure 14. As before, the most notable difference in the pressure distribution is found when the free surface level in the gap is lowest ($t = 41.50 T$). This time instant also marks the minimum of the dynamic force on the right side of Figure 6.

Figure 15 shows the relative velocity fields close to the intersection of free surface and body resulting from the inviscid and viscous FVM calculations at that time instant. Beside the different level of the free surface, a vortex formation can be observed in case of viscous flow assumptions. A fact that may favour the vortex generation is that the body has reached its maximum downward velocity at that time instant while the fluid in the gap is starting to move upward. Although a clear influence of viscosity can be observed in the flow field, the impact on the first order force component is relatively low with 2.0% (see Table 3). The impact of viscosity on the second order force component is somewhat more pronounced with 5.2%.

From the relatively low influence of viscosity it is concluded that the highly nonlinear relation between body motion and hydrodynamic forces observed in this study are mainly induced by the free surface. This finding is in contrast to investigations on hulls sections with rectangular shape, which often indicate that a linearised free surface representation can be sufficiently accurate while viscosity has a strong influence (e.g. Kristiansen and Faltinsen (2012)). A likely reason is that the relevance of vortex shedding is much more pronounced when the edges of the body are sharp (Moradi et al., 2015). At the same time, less horizontal velocities are induced when the walls in the gap are exclusively vertical, possibly leading to a decreased relevance of nonlinear free surface representations.

It is well possible that the relevance of viscosity for the semi-circular hull shape will be higher if the motion amplitude is further increased. According to the results given by Bonfiglio and Brizzolara (2018), who investigated the problem up to a motion amplitude of $z_A = a/3$ using a viscous FVM, the flow would also be strongly characterized by wave breaking phenomena in this case. Although the BEM in combination with the MEL approach is capable of capturing very steep waves, phenomena like wave breaking and air inclusions can not be accounted for. At this point the boundary element method would reach its limit not only because it neglects viscosity, but also because the free surface can not be tracked anymore in a physically meaningful way. Taking into consideration that the free surface already reaches very close to the bottom of the hull in certain time instances (e.g. $\omega = 0.77\sqrt{g/a}, t = 41.50 T$ in Figure 12) higher motion amplitudes were regarded out of scope for this study.

Another factor that may increase the relevance of viscosity are very small hull distances (Zhao et al., 2018)). The hull distance that was chosen in this study corresponds to the closest hull distance which was experimentally studied by Wang and Wahab (1971). It is believed to be a realistic lower limit for practical hull distances of multi-hull ships. For instance the ratio between gap size and draft of the catamaran examined by Lugni et al. (2004) was 1.625, whereas in the case investigated here it was 1.0.

6. Conclusion

A numerical study on the heave radiation problem of a twin-hull section with semi-circular shape was carried out. Three different numerical approaches were used to solve the flow problem in time-domain: A nonlinear boundary element method, a finite volume method incorporating inviscid flow assumptions and a finite volume method incorporating viscous flow assumptions. Focus was laid on frequencies at which piston-like resonant flow occurred in the

gap between the hulls. First order force components were validated against existing experimental measurements and compared to published results from linear potential theory. Subsequently, the forces and free surface elevation in the gap resulting from the different numerical approaches were compared in detail at three frequencies and two motion amplitudes respectively. Based on the results the following conclusions are drawn:

- All three approaches are able to predict valid added mass and damping coefficients for the presented problem and show a significant improvement over linearised potential methods in that regard. The strong variation of hydrodynamic coefficients goes along with a change of the phase shift between body motion and fluid motion in the gap.
- The nonlinear characteristics of the dynamic force predicted by the three approaches are in very good agreement: A significant influence of second order force components is found with the corresponding phase angle varying strongly over frequency. Significance of higher order force components seem to increase with motion amplitude. The free surface in the gap is considered the main cause for nonlinearity in the cases examined.
- Deviations between the dynamic force predicted by BEM and FVM are mainly associated with a different prediction of the free surface elevation in vicinity to the body. Thus, an accurate representation of the free surface shape is considered highly relevant for a numerical analysis of the problem, in particular when the free surface is close to the bottom of the hull.
- Impact of viscosity on the dynamic forces was found to be relatively low throughout the examined cases. Vortex shedding in vicinity of the intersection between body and free surface was found in one case which had an impact on the pressure distribution in that time instant. However, the dynamic force amplitudes were still in good agreement.

All in all, the study demonstrates that the nonlinear dependence of forces on body motion associated with the radiation problem of twin-hulls with semi-circular shape at low to moderate motion amplitudes can be recovered well using inviscid methods. Thus, the nonlinear boundary element method presented here is considered a suitable tool for the analysis of piston mode resonance phenomena associated with bodies of rather round shape and feasible alternative to more elaborate tools like the finite volume method. Future studies may investigate the effects of viscosity for a variety of common hull shapes. Also, motion excitation in different degrees of freedom by external waves may be considered, preparing an application of the BEM in 2D+t based seakeeping analyses of multi-hull ships.

Acknowledgement

The authors are very grateful for the funding awarded by the German Federal Ministry of Defence under the administration of the Technical Centre for Ships and Naval Weapons, Maritime Technology and Research (WTD 71). The authors sincerely thank Dr. Norbert Stuntz for providing a valuable technical feed-back and for fruitful discussions. Two anonymous peer reviewers are thanked for their critical reading and mindful comments which helped a lot to increase the quality of this article.

References

- Ananthakrishnan, P., 2015. Viscosity and nonlinearity effects on the forces and waves generated by a floating twin hull under heave oscillation. *Applied Ocean Research* 51, 138 – 152. doi:10.1016/j.apor.2015.03.002.
- Bonfiglio, L., Brizzolara, S., 2018. Amplitude induced nonlinearity in piston mode resonant flow: A fully viscous numerical analysis. *Journal of Offshore Mechanics and Arctic Engineering* 140. doi:10.1115/1.4037487.
- Faltinsen, O.M., Rognabakke, O.F., Timohka, A.N., 2007. Two-dimensional resonant piston-like sloshing in a moonpool. *Journal of Fluid Mechanics* 575, 359–397. doi:10.1017/S002211200600440X.
- Greco, M., 2001. A Two-dimensional Study of Green-Water Loading. Ph.D. thesis. Norwegian University of Science and Technology. Trondheim, Norway.
- Haase, H., Soproni, J.P., Abdel-Maksoud, M., 2015. Numerical analysis of planing boats in head waves using a 2d+t method. *Ship Technology Research* 62, 131–139. doi:10.1179/2056711115Y.0000000003.
- Kristiansen, T., Faltinsen, O.M., 2010. A two-dimensional numerical and experimental study of resonant coupled ship and piston-mode motion. *Applied Ocean Research* 32, 158–176. doi:10.1016/j.apor.2009.10.001.
- Kristiansen, T., Faltinsen, O.M., 2012. Gap resonance analyzed by a new domain-decomposition method combining potential and viscous flow. *Applied Ocean Research* 34, 198–208. doi:10.1016/j.apor.2011.07.001.

- Lee, C.M., Jones, H., Bedel, J.W., 1971. Added mass and damping coefficients of heaving twin cylinders in a free surface. Technical Report 3695. Naval Ship Research and Development Center. Bethesda, MD, USA.
- Lewandowski, E.M., 1992. Hydrodynamic forces and motions of a cylinder near a vertical wall. *Journal of Ship Research* 36, 248–254.
- Li, Y., Zhang, C., 2016. Analysis of wave resonance in gap between two heaving barges. *Ocean Engineering* 117, 210–220. doi:10.1016/j.oceaneng.2016.03.042.
- Longuet-Higgins, M.S., Cokelet, E.D., 1976. The deformation of steep waves on water I. A numerical method of computation. *Proceedings of the Royal Society A* 350, 1–26.
- Lugni, C., Colagrossi, A., Landrini, M., Faltinsen, O., 2004. Experimental and numerical study of semi-displacement mono-hull and catamaran in calm water and incident waves, in: *Proceedings of the 25th Symposium on Naval Hydrodynamics*, St. John's, Canada. August 8–13.
- Maiti, S., Sen, D., 2001. Nonlinear heave radiation forces on two-dimensional single and twin hulls. *Ocean Engineering* 28, 1031 – 1052. doi:10.1016/S0029-8018(00)00043-3.
- McIver, M., 1996. An example of non-uniqueness in the two-dimensional linear water wave problem. *Journal of Fluid Mechanics* 315, 257–266. doi:10.1017/S0022112096002418.
- McIver, M., McIver, P., 2016. The added mass for two-dimensional floating structures. *Wave Motion* 64, 1–12. doi:10.1016/j.wavemoti.2016.02.007.
- McIver, P., McIver, M., Zhang, J., 2003. Excitation of trapped water waves by the forced motion of structures. *Journal of Fluid Mechanics* 494, 141–162. doi:10.1017/S0022112003005949.
- McIver, P., Porter, R., 2016. The motion of a freely floating cylinder in the presence of a wall and the approximation of resonances. *Journal of Fluid Mechanics* 795, 581–610. doi:10.1017/jfm.2016.201.
- Molin, B., 2001. On the piston and sloshing modes in moonpools. *Journal of Fluid Mechanics* 430, 27–50. doi:10.1017/S0022112000002871.
- Moradi, N., Zhou, T., Cheng, L., 2015. Effect of inlet configuration on wave resonance in the narrow gap of two fixed bodies in close proximity. *Ocean Engineering* 103, 88–102. doi:10.1016/j.oceaneng.2015.04.063.
- Nordenstrøm, N., Faltinsen, O., Pedersen, B., 1971. Prediction of wave-induced motions and loads for catamarans, in: *Offshore Technology Conference*, Houston, Texas, 19–21 April. doi:10.4043/1418-MS.
- Ohkusu, M., 1969. On the heaving motion of two circular cylinders on the surface of a fluid. *Reports of Research Institute for Applied Mechanics* 17, 167–185.
- Porter, R., Evans, D.V., 2011. Estimation of wall effects on floating cylinders. *Journal of Engineering Mathematics* 70, 191–204. doi:10.1007/s10665-010-9420-x.
- Simonis, H., Marleaux, P., Abdel-Maksoud, M., 2020. Numerical analysis of semi-displacement vessels in head waves, in: *Proceedings of the 33rd Symposium on Naval Hydrodynamics*, Osaka, Japan. October 18–23.
- Sun, H., 2007. A Boundary Element Method Applied to Strongly Nonlinear Wave-Body Interaction Problems. Ph.D. thesis. Norwegian University of Science and Technology. Trondheim, Norway.
- Ursell, F., 1949. On the heaving motion of a circular cylinder on the surface of a fluid. *The Quarterly Journal of Mechanics and Applied Mathematics* 2, 218–231. doi:10.1093/qjmath/2.2.218.
- Wang, S., Wahab, R., 1971. Heaving oscillations of twin cylinders in a free surface. *Journal of Ship Research* 15, 33–48.
- Yeung, R.W., Seah, R.K.M., 2007. On helmholtz and higher-order resonance of twin floating bodies. *Journal of Engineering Mathematics* 58, 251–265. doi:10.1007/s10665-006-9109-3.
- Zhao, W., Pan, Z., Lin, F., Li, B., Taylor, P.H., Efthymiou, M., 2018. Estimation of gap resonance relevant to side-by-side offloading. *Ocean Engineering* 153, 1–9. doi:10.1016/j.oceaneng.2018.01.056.